Global mapping of topography on the 660-km discontinuity

Peter M. Shearer & T. Guy Masters

Institute of Geophysics and Planetary Physics, Scripps Institution of Oceanography, University of California, San Diego, La Jolla, California 92093, USA

Long-period precursors to the SS seismic phase are used to produce global maps of topography for the discontinuity at 660 km depth in the upper mantle. These maps indicate discontinuity depth variations of up to 30 km and suggest a correlation between regional depressions in the 660-km discontinuity and subduction zones — a result more consistent with models in which the subducting slabs are deflected horizontally at the discontinuity than with models of unhindered slab penetration into the lower mantle.

MANY of the fundamental unresolved questions in mantle chemistry and dynamics hinge on the properties of the Earth's 660-km discontinuity in seismic velocities. Advocates of whole-mantle convection suggest that the discontinuity represents a mineral phase change alone which causes little or no resistance to convection, whereas others favour a change in composition near 660 km which separates the mantle into two convection regimes. For the whole-mantle model, downgoing slabs in subduction zones penetrate through the 660-km discontinuity into the lower mantle; in the layered-mantle model the slabs encounter resistance near 660 km which prevents penetration. Intermediate models have also been proposed in which the 660-km discontinuity is a partial barrier to convection[1,2]. Detailed knowledge of any depth variations of the 660-km discontinuity would help to discriminate between these models, as they predict different patterns of discontinuity topography.

The existence of a sharp jump in seismic velocities near 660 km depth has been known for over 25 years[3,4]. High-pressure experiments in mineral physics have shown that the bulk of this velocity jump can be explained by the phase change γ-olivine (spinel) → perovskite + magnesiowüstite[5-7]. But controversy remains[8-10] about whether a change in composition might also occur at or near 660 km. The presence of a compositional density contrast would inhibit convection across the boundary. Even without such a change in chemistry, slabs may encounter some resistance near 660 km due to a viscosity contrast at the discontinuity[11] and the negative Clapeyron slope (the change in pressure with temperature, $\gamma_{660} = dP/dT$) for the 660-km phase change[2,12]. Values for γ_{660} obtained from mineral physics experiments can be used to relate variations in mantle temperature to differences in discontinuity depths; colder temperatures should cause the discontinuity to move to deeper depths.

In principle, seismic travel times can be used to obtain the velocity structure near where the subducting slabs intersect the 660-km discontinuity in order to resolve whether the slabs penetrate to the lower mantle. But results have been inconsistent, with some studies finding evidence for deep slab penetration[13-18], whereas others[19-21] seem to image the horizontal deflection of slabs in some areas near 660 km. Another approach is to study directly the behaviour of the 660-km discontinuity near the subducting slabs by examining reflected and converted phases from the discontinuity[22,23]. In practice this has been hindered by the difficulty of observing these relatively low-amplitude seismic arrivals. Recently, however, processing techniques have been developed that permit these arrivals to be seen fairly routinely in long-period seismograms[22,24-26].

Here we examine long-period precursors to SS which result from underside reflections from the 660-km discontinuity. These S660S phases are ideally suited for studying global variations in discontinuity topography because of their wide distribution of bounce points. Previous analysis of S660S arrivals[26] showed that there are only small differences in discontinuity depths between different tectonic regions and suggested the presence of a 20-km depression in the vicinity of the subduction zones in the northwest Pacific. We now extend this analysis to a larger data set and directly map the 660-km discontinuity topography without dividing the data into different tectonic regions. Maps obtained from analysis of more than 3,000 seismograms indicate large-scale coherent patterns of discontinuity topography with depth variations of up to 30 km. Regional depressions in the 660-km discontinuity seem to be associated with subduction zones, with the position and broad extent of these depressions supporting models in which the subducting slabs break up or are deflected horizontally at 660 km rather than models of unhindered slab penetration.

Precursors to SS

We examine long-period transverse-component seismograms at source–receiver ranges from 80° to 180° obtained from the Global Digital Seismograph Network between 1976 and 1987 and select more than 4,000 traces with high-quality SS arrivals from shallow events (<75 km deep). Figure 1*a* shows the result of stacking these waveforms after normalizing and aligning the SS arrival at zero time as a reference phase. Amplitudes in the stacked image are indicated by colours; the maximum amplitude shown is only 0.05 of the SS wave amplitude. Figure 1*b* shows the predicted arrival times of seismic phases relative to SS as obtained by ray tracing through a reference model of the Earth[27]. The prominent blue streaks seen 2.5 to 4 min before SS are precursors resulting from underside reflections off upper-mantle discontinuities. The reflections from the 410- and 660-km discontinuities, S410S and S660S, are identified in Fig. 1*b*. The stacked image also shows an apparent arrival from a reflector between 410 and 660 km, corresponding to a discontinuity at 520 km depth[25]. The other discontinuity phases labelled in Fig. 1*b* are only marginally visible in Fig. 1*a*.

Here we consider only the S660S phase; some results for S410S and other discontinuity phases have been described elsewhere[26]. Figure 2 shows the ray geometry of S660S compared with S and SS ray paths. S660S is ideally suited for examining discontinuity topography as it is associated with a single reflection point on the 660-km discontinuity. In contrast, most other discontinuity phases result from several different possible ray paths and reflection points, greatly complicating their interpretation. Figure 3 shows S660S bounce points from 3,139 seismograms between 110° and 180°. Although some areas of sparse sampling exist, reasonable global coverage is obtained, with the Pacific and Indian Oceans being particularly well sampled. To find possible S660S phases on individual seismograms, we calculate the cross-correlation function between the SS arrival and the remainder of the seismogram (details of this method are described in ref. 26). This procedure obtains travel times and amplitudes of apparent S660S arrivals relative to the SS travel

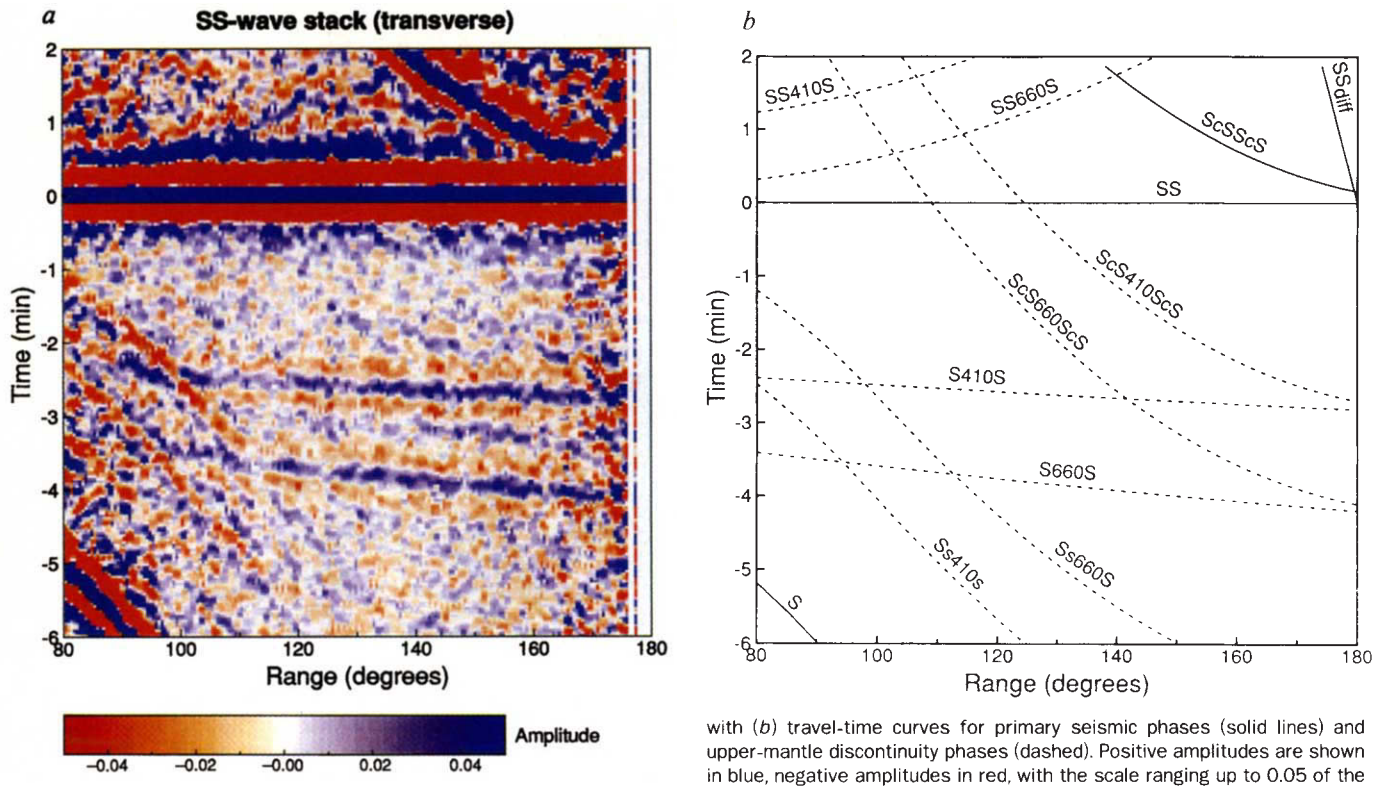

FIG. 1 *a*, Stacked colour image of more than 4,000 long-period transverse-component seismograms from the Global Digital Seismic Network, compared with (*b*) travel-time curves for primary seismic phases (solid lines) and upper-mantle discontinuity phases (dashed). Positive amplitudes are shown in blue, negative amplitudes in red, with the scale ranging up to 0.05 of the maximum amplitude of the SS reference phase. We examine the S660S phase, which arrives 3.5–4 min before SS and results from an underside reflection off the 660-km discontinuity.

time. These SS − S660S differential travel times are directly sensitive to the two-way travel time between the discontinuity and the surface (see Fig. 2), and, assuming an upper-mantle velocity model, can be converted to apparent discontinuity depths.

Discontinuity depths measured in this way will be biased by any lateral velocity variations in the upper mantle, and must be corrected. For example, a slow region above the 660-km discontinuity would increase the SS − S660S travel time and increase the apparent depth of the 660-km discontinuity. A direct measure of vertical travel time differences through the upper mantle may be obtained from SS − S times. These phases have nearly identical ray paths near the source and receiver, but SS has two additional legs through the upper mantle near the SS bounce point (see Fig. 2). Because recent global velocity inversions have indicated that heterogeneity in the mantle below 660 km is relatively small compared with differences above 660 km, the SS − S travel times provide a good estimate of the upper-mantle velocity variations at the SS bounce point. We use a smoothed version of SS − S residuals obtained by Woodward and Masters[28] to correct our observed SS − S660S residuals. Analysis of the 410-km phases is complicated by the effects of transition-zone heterogeneity and is deferred to future work.

Topography of the 660-km discontinuity

In principle, 660-km discontinuity depths could be obtained for each of the S660S bounce points shown in Fig. 3. Because of the large scatter in observed arrival times, however, stable estimates of discontinuity depths are only possible when results are averaged from a number of seismograms. Figure 4*a* shows the variations in 660-km discontinuity depths (relative to a mean depth of 659 km) obtained for 416 caps spaced ~10° apart. Within each cap, results are combined from all S660S bounce points within a 10° radius, and the mean apparent depth to the 660-km discontinuity and its standard error are calculated with a bootstrap technique[29]. Only caps with standard errors in depth less than 10 km are shown in Fig. 4*a*, with the gaps in the spatial coverage generally corresponding to areas with little or no data. Large-scale coherent patterns of discontinuity topography are seen with peak-to-peak amplitudes of ~30 km.

The depth variations shown in Fig. 4*a* correspond to differences in the relative arrival times of S660S and SS. Conceivably these times could be biased by effects other than discontinuity topography. Probably the largest potential source of error is inaccuracies in the corrections for lateral heterogeneity, as these will directly affect the apparent depths that we calculate. The gross structures shown in Fig. 4 are most reliably resolved, because the SS − S residual pattern used for the corrections is well constrained at large scales. Improved velocity models will, however, almost certainly result in some changes to the finer details seen in Fig. 4. Another possibility is that a small discontinuity of fluctuating brightness or depth exists near the 660-km discontinuity, biasing S660S travel times by variable amounts. If so, one might expect to see some correlation between apparent discontinuity depths and the amplitude of discontinuity reflections. Amplitudes of the S660S phases presented here are not correlated to the apparent depths to the 660-km discontinuity, although such a correlation has been noted in ScS reverberation data[24].

Using the method of spherical splines[28,30], we used these cap-averaged depths and their standard errors to produce a smooth model of discontinuity topography (Fig. 4*b*). This technique gives the surface with smallest second lateral derivative integrated over the sphere for a given target χ^2. The model

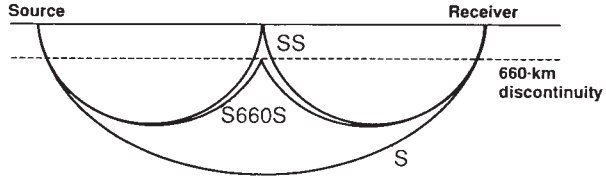

FIG. 2 The ray geometry for S, SS and S660S. The ray paths of SS and S660S are nearly identical except that the S660S bounce point is at the 660-km discontinuity rather than the surface.

TABLE 1 Spherical harmonic coefficients for model Topo660a

		$m=0$	1	2	3	4	5	6	7	8
C_0^m		658.537								
	S_0^m	0.000								
C_1^m		1.036	−0.691							
	S_1^m	0.000	−0.922							
C_2^m		−0.973	0.225	0.896						
	S_2^m	0.000	2.506	−1.731						
C_3^m		0.555	0.225	0.258	−0.011					
	S_3^m	0.000	1.981	0.688	0.494					
C_4^m		−0.204	−1.217	−0.022	0.735	−0.458				
	S_4^m	0.000	−0.783	−0.901	0.790	−0.426				
C_5^m		0.806	−0.278	0.651	0.077	−0.265	−0.254			
	S_5^m	0.000	0.172	−0.617	−0.115	−0.250	−0.317			
C_6^m		−0.153	−0.241	0.189	0.199	0.035	0.281	0.300		
	S_6^m	0.000	−0.225	−0.386	0.277	−0.189	−0.546	0.349		
C_7^m		0.141	−0.017	0.285	0.194	−0.160	0.157	−0.112	−0.116	
	S_7^m	0.000	0.116	0.082	−0.042	−0.439	−0.374	0.328	0.116	
C_8^m		−0.157	0.015	−0.130	0.266	−0.047	−0.246	0.029	−0.179	0.162
	S_8^m	0.000	−0.060	0.124	0.117	0.358	0.268	0.240	−0.178	−0.074

Spherical harmonic coefficients up to degree 8 for the model of discontinuity topography shown in Fig. 4*b*. We have normalized the coefficients using the convention described in ref. 56.

shown fits the 340 cap-averaged depths with a χ^2 of 300. Changing the target χ^2 so that the data are substantially over- or underfitted results in maps of similar shape to that in Fig. 4*b* but with variable amplitude. The equivalent spherical harmonic expansion of this surface has nearly all its power in the first eight harmonic degrees (Table 1) and is dominated by harmonic degree 2. Unlike simple spherical harmonic expansions, the spherical spline method does not produce models with large structure in regions with no data. The topography shown in Fig. 4*b* should not, however, be taken at face value without comparison with Fig. 4*a* to see where the data actually constrain the model.

The 660-km discontinuity is anomalously deep in regions northwest of the Japan and Kuril–Kamchatka trenches, west of the Tonga trench, and in eastern South America. Depths are generally shallow beneath North America, Antarctica and the Indian Ocean. The data coverage in the northwest Pacific is especially good and clearly resolves a 15–20-km-deep trough in the 660-km discontinuity which is ~1,500 km wide and 5,000 km long. The corrections for upper-mantle heterogeneity from the SS−S times are relatively small in this region; this feature is also apparent in the uncorrected data. This trough is oriented parallel to the Kuril–Kamchatka subduction zone but is displaced to the northwest. The depressions west of Tonga and in eastern South America are also near subduction zones, but should be considered less reliable anomalies, as the Tonga feature is constrained by comparatively little data and the South American depression is largely determined by the corrections for fast upper-mantle velocities in this area. It is possible that additional topographic lows occur for other subduction zones in the western Pacific, but the data coverage is too sparse to resolve discontinuity depths in this region.

Transition zone temperature variations

Large-scale topographic variations on the 660-km discontinuity seem to be about ~30 km in peak-to-peak amplitude, consistent with results from other discontinuity phases and ScS reverberations. Measured values of the Clapeyron slope for the phase change γ-olivine (spinel) → perovskite + magnesiowüstite near 660 km have ranged from −2 to −4 MPa K^{-1} (refs 31–33). The negative Clapeyron slopes imply an endothermic reaction in which the discontinuity moves downwards at lower temperatures. These values predict that every 100-K decrease in mantle temperature will cause a 5–10-km increase in depth to the 660-km discontinuity. Thus, lateral differences in mantle temperature at 660 km between 300° and 600° are required to explain the observed 30 km of discontinuity topography directly in terms of the Clapeyron slope, with the topographic highs and lows representing warmer and cooler regions respectively.

Because temperature variations affect seismic velocities, one might expect these features to show up in global inversions for transition-zone velocity structure. For some time, these inversions[34–37] have indicated the presence of a large anomaly of spherical harmonic degree 2 in the transition zone, with fast velocities centred in the western Pacific and eastern South America. The latter feature is roughly consistent with the 660-km depression seen in the maps of discontinuity topography (Fig. 4), but the western Pacific anomaly (centred east of the Philippines) is not reproduced in these maps. Few data exist in this area, so it is unlikely that a significant depression in this area could be resolved with the S660S phases considered here. ScS reverberation data[24] have much better coverage in this region, but also do not show a significant depression in the 660-km discontinuity.

The most clearly resolved feature in the S660S data is the trough in the 660-km discontinuity behind the Kuril–Kamchatka subduction zone. Global models of transition-zone velocity do not show anomalies specific to this region, although in some models the western Pacific high-velocity zone extends to the north of Japan. The high in the 660-km topography near Antarctica is in reasonable agreement with a slow region in the velocity models, but highs over the Indian Ocean and northern North America do not seem correlated with velocity features. Comparisons between discontinuity topography and mantle velocity models should be made with care, as the models have different vertical and horizontal resolution. The global velocity inversions

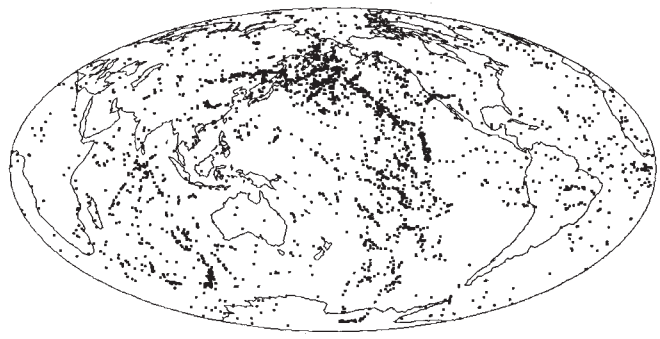

FIG. 3 The global distribution of S660S bounce points at source–receiver ranges between 110° and 180°. Estimates of 660-km discontinuity depths can be made at each of these points, but in practice stable results are obtained only by averaging results from many points.

have limited depth resolution and give only average anomalies within a broad depth range, whereas variations in 660-km discontinuity depth are sensitive only to the temperature at the discontinuity itself. In addition, the models are not derived independently, as knowledge of upper-mantle velocities is necessary to correct apparent discontinuity depths for the integrated effect of heterogeneity between the surface and 660 km.

Northwest Pacific subduction zones

The data coverage near the subducting slabs in the northwest Pacific is dense enough for a more detailed examination of discontinuity topography in this area. Figure 5 is a close-up of this region and shows the location of the S660S bounce points and the subduction zone seismicity. Earthquake locations from the International Seismological Centre (ISC) from 1970 to 1987 are shown, with crosses for events between 100 and 400 km depth and squares for events deeper than 400 km. These earthquakes define the Wadati-Benioff zones which outline the position of the subducting slabs. The line labelled AB defines a great-circle cross-section through this region; the adjacent lines are 5° away. These lines are chosen to enclose a significant number of the S660S bounce points rather than to be exactly orthogonal to the Kuril-Kamchatka subduction zone.

S660S data are binned by range along AB, and discontinuity depth estimates obtained for each range bin. Figure 6 shows the resulting 660-km discontinuity depths and standard error bars for both the raw and SS−S corrected data. Depths are shown at 3° range increments with each point including data within a window of 6° range. A 20-km-deep depression is seen in the 660-km discontinuity, consistent with the position of the trough shown in Fig. 4. This feature is also apparent in the uncorrected depths, but its shape is distorted by a gradient in integrated upper-mantle velocities along the cross-section. The top plot also shows ISC earthquake locations (1970–87) within 3° of AB. The event at 611 km is the 12 May 1990 Sakhalin Island earthquake[38]. Because the cross-section crosses the Kuril-Kamchatka subduction zone rather obliquely, some broadening is seen in the Wadati-Benioff zone, which appears nearly vertical because of the large vertical exaggeration. In addition, this profile is near the corner between the Kuril and Japan subduction zones, complicating any interpretation of slab geometries. It is clear, however, that the bulk of the depression in the 660-km discontinuity is offset to the northwest from the point at which the projection of the subducting slabs intersects the discontinuity.

The depression appears to be ~15° (1,700 km) across and ~20 km deep. The lateral resolution of the long-period S660S phase (~25-s period) is limited to features larger than ~10°. In particular, these data cannot exclude the possibility of a large deflection in the 660-km discontinuity in the immediate vicinity of subducting slabs if this feature were only a few degrees across. The edge of the trough could be fairly sharp, particularly on the southeastern side (note that this sharpness is lost in the smooth map of topography shown in Fig. 4). There is a suggestion in the cross-section (Fig. 6) that the 660-km discontinuity may be slightly higher in areas immediately adjacent to the trough than regions further away. But, considering the size of the error bars and the absence of this feature in the cap averages (Fig. 4), the existence of these highs is very uncertain.

Slab penetration?

The idea that the subducting slabs in the northwest Pacific penetrate the 660-km discontinuity is controversial. Residual sphere analyses of both S-waves and P-waves for deep focus events have revealed patterns consistent with penetration of the Kuril slab to depths of 900 km or more[13,14], but it has been argued that these patterns are caused by deep-mantle or near-receiver anomalies unrelated to the slab structure[39–42]. Waveform and amplitude anomalies have also been used to infer deep slab penetration in the Kurils[18,43], but these interpretations have been questioned[41,44,45]. Three-dimensional P-wave velocity inversions from ISC travel times for structure in this region have found evidence both for deep slab penetration[17] and the horizontal deflection of slabs near 660 km (ref. 19). A study that used both direct P and surface-reflected pP travel times found evidence for both types of structures, with deep slab anomalies imaged in the nothern Kurils and near-horizontal features seen in the Japan and Izu-Bonin arcs[20]. Recent work combining whole-mantle and regional inversion for western Pacific structure[21] appears to resolve horizontal slab features west of the southern Kuril to Izu-Bonin arcs which extend more than 1,000 km. The regional depression in the 660-km discontinuity behind the Kuril subduction zone (Figs 4 and 6) supports those models in which the cold, subducting slab spreads out horizontally near 660 km rather than models of unhindered slab penetration.

A similar debate has occurred over the fate of subducting slabs in the Tonga region. The complex geometry and focal mechanisms of deep earthquakes from the Tonga subduction zone may indicate that the slabs encounter resistance near 660 km and are displaced horizontally[46,47]. Alternatively, the contortions in the Tonga slab may be due to local tectonic

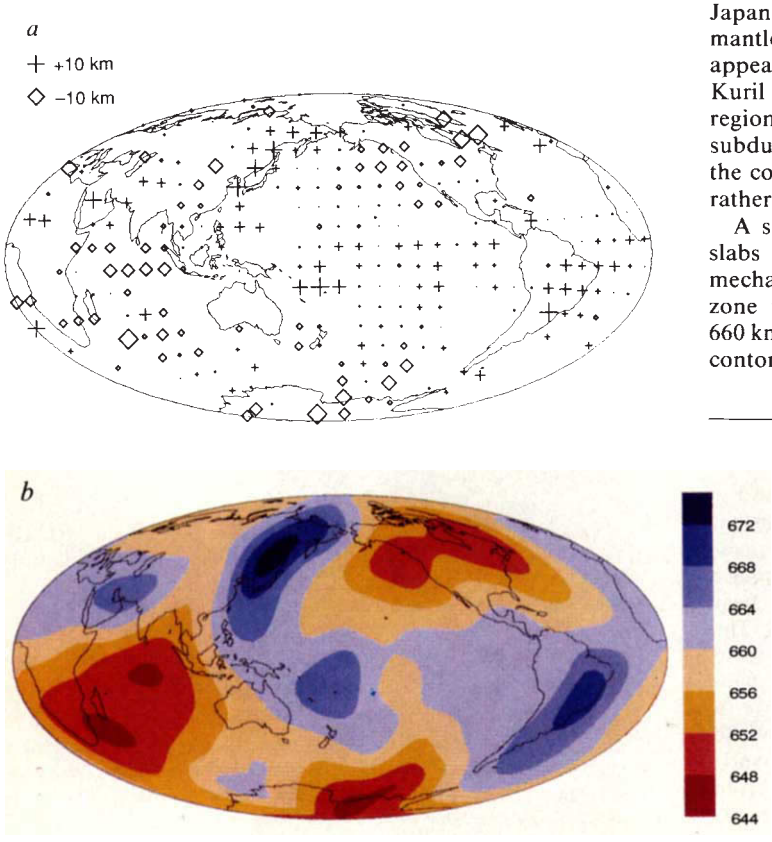

FIG. 4 *a*, Average depths to the 660-km discontinuity obtained for data within caps of 10° radius (relative to a mean depth of 659 km). Only cap averages with standard errors less than 10 km are plotted. *b*, Smooth map of topography on the 660-km discontinuity obtained using the method of spherical splines on the cap averages shown in *a*. Peak-to-peak topography variations are ~30 km. Note the depressions in the 660-km discontinuity north of Japan, west of Tonga, and in eastern South America.

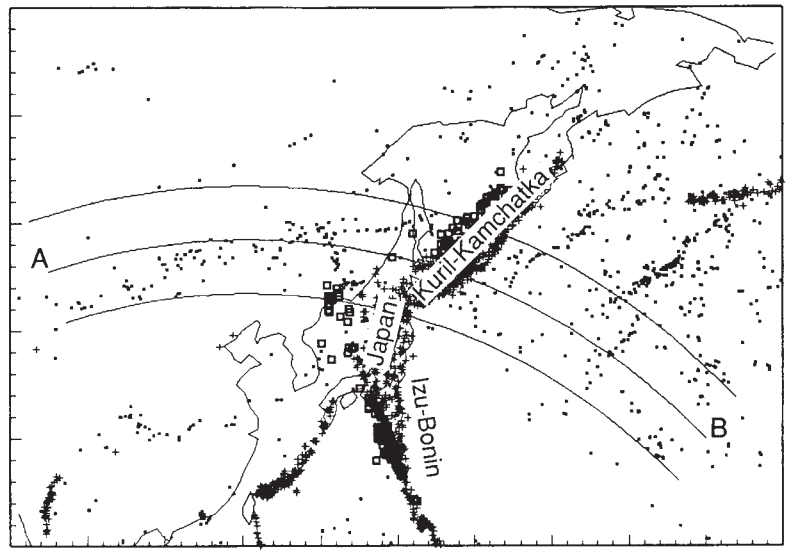

FIG. 5 S660S bounce points and seismicity in the northwestern Pacific and eastern Asia (■, S660S bounce points; +, earthquakes between 100 and 400 km; □, earthquakes deeper than 400 km). The curve labelled AB is a great circle that defines the cross-section shown in Fig. 6; the adjacent curves are 5° away.

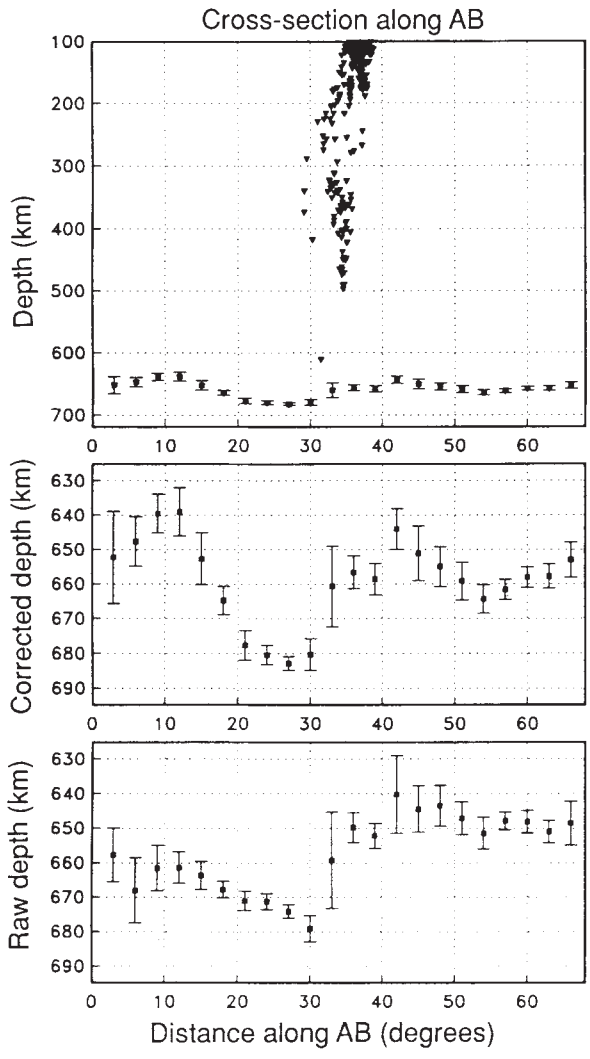

FIG. 6 Depths to the 660-km discontinuity and seismicity along a cross-section through the Kuril–Kamchatka subduction zone (the line AB in Fig. 5), showing results from both raw SS − S660S times (bottom plot) and depths corrected for the effects of upper-mantle heterogeneity (top plots). Note the depression, ~15° wide, in the 660-km discontinuity just behind where the projection of the subducting slab seems to intersect the discontinuity.

interactions and may not necessarily require resistance to penetration at 660 km (ref. 48). Some travel-time studies[16,49–51] from deep-focus events have found evidence for high-velocity anomalies consistent with deep slab penetration whereas others have not[52,53]. The suggestion of a regional depression in the 660-km discontinuity behind the Tonga subduction zone (Fig. 4) supports the idea that at least some of the subducted lithosphere has been deposited at this depth. Evidence for this depression is not conclusive, as it is constrained by only a few S660S phases and the SS − S corrections for upper-mantle structure are also sparse in this area. Another depression in the 660-km discontinuity is seen in eastern South America, and may be related to subduction beneath the Andes. This feature is not clear in the raw S660S times but results from the corrections for the fast upper-mantle velocities in this region.

If the 660-km discontinuity is entirely a compositional change, modelling results have shown that it should be displaced several hundred kilometres or more by subducting slabs[12,54]. Our S660S results and other recent observations[23,24] are clearly inconsistent with such large depth variations, and support the idea that most of the jump in seismic velocities near 660 km results from a phase change. The possibility of a small chemical change in density at or near 660 km cannot be ruled out, because even large perturbations to its depth might not be seen in seismic observations. Even in the absence of a compositional density change at 660 km, the subducting slabs will encounter some resistance to penetration because of the negative Clapeyron slope of the 660-km phase change and the likely existence of a viscosity contrast near 660 km (ref. 11). Recent modelling results[2] have indicated that a Clapeyron slope of $\gamma_{660} = -4$ MPa K^{-1} will result in layered convection, with a mixture of whole-mantle and layered convection occurring for $\gamma_{660} = -2$ MPa K^{-1}.

Our results suggest a correlation between subduction zones and broad regional depressions in the 660-km discontinuity. The existence of these depressions is consistent with models in which the descending slabs in many areas are deflected horizontally to create large areas of moderately cooler temperatures behind subduction zones. Such models would include the hypothesis of a gravitationally trapped megalith[55] and some numerical simulations of subducting slabs encountering a viscosity contrast[11]. The possibility of localized regions of deep slab penetration, as suggested by some velocity inversions, cannot be excluded. In addition, the data are currently insufficient to determine whether these discontinuity depressions are a general feature beneath all deep subduction zones, or are specific to certain regions. □

Received 24 October 1991; accepted 24 January 1992.

1. Silver, P. G., Carlson, R. W. & Olson, P. *Ann. Rev. Earth planet. Sci.* **16,** 477–541 (1988).
2. Machetel, P. & Weber, P. *Nature* **350,** 55–57 (1991).
3. Niazi, M. & Anderson, D. L. *J. geophys. Res.* **70,** 4633–4640 (1965).
4. Johnson, L. R. *J. geophys. Res.* **72,** 6309–6325 (1967).
5. Liu, L.-G. *Nature* **262,** 770–772 (1976).
6. Jackson, I. *Earth planet. Sci. Lett.* **62,** 91–103 (1983).
7. Ito, E., Takahashi, E. & Matsui, Y. *Phys. Earth planet. Inter.* **67,** 238–248 (1984).
8. Jeanloz, R. in *Mantle Convection: Plate Tectonics and Global Dynamics* (ed. Peltier, W. R.) 203–259 (Gordon and Breach, New York, 1989).
9. Duffy, T. S. & Anderson, D. L. *J. geophys. Res.* **94,** 1895–1912 (1989).
10. Jeanloz, R. *Geophys. Res. Lett.* **18,** 1743–1746 (1991).
11. Gurnis, M. & Hager, B. H. *Nature* **335,** 317–321 (1988).
12. Christensen, U. R. & Yuen, D. A. *J. geophys. Res.* **89,** 4389–4402 (1984).
13. Jordan, T. H. *J. geophys. Res.* **43,** 473–496 (1977).
14. Creager, K. C. & Jordan, T. H. *J. geophys. Res.* **89,** 3031–3049 (1984).
15. Creager, K. C. & Jordan, T. H. *J. geophys. Res.* **91,** 3573–3589 (1986).
16. Fischer, K. M., Creager, K. C. & Jordan, T. H. *J. geophys. Res.* **96,** 14403–14427 (1991).
17. Kimaya, S., Miyatake T. & Hirahara, K. *Geophys. Res. Lett.* **15,** 829–831 (1988).
18. Suetsugu, D. *J. Phys. Earth* **37,** 265–295 (1989).
19. Zhou, H. & Clayton, R. W. *J. geophys. Res.* **95,** 6829–6851 (1990).
20. van der Hilst, R., Engdahl, R., Spakman, W. & Nolet, G. *Nature* **353,** 37–43 (1991).
21. Fukao, Y., Obayashi, M., Inoue, H. & Nenbai, M. *J. geophys. Res.* (in the press).
22. Revenaugh, J. & Jordan, T. H. *J. geophys. Res.* **94,** 5787–5813 (1989).
23. Richards, M. A. & Wicks, C. W. *Geophys. J. Int.* **101,** 1–35 (1990).
24. Revenaugh, J. & Jordan, T. H. *J. geophys. Res.* **96,** 19763–19780 (1991).
25. Shearer, P. M. *Nature* **344,** 121–126 (1990).
26. Shearer, P. M. *J. geophys. Res.* **96,** 18147–18182 (1991).
27. Dziewonski, A. M. & Anderson, D. L. *Phys. Earth planet. Inter.* **25,** 297–356 (1981).
28. Woodward, R. L. & Masters, G. *J. geophys. Res.* **96,** 6351–6377 (1991).
29. Efron, B. & Tibshirani, R. *Science* **253,** 390–395 (1991).
30. Shure, L., Parker, R. L. & Backus, G. E. *Phys. Earth planet. Inter.* **28,** 215–229 (1982).
31. Ito, E. & Yamada, H. *High-Pressure Research in Mineral Physics* (ed. Akimoto, S. & Manghnani, M. H.) 405–419 (Center for Academic Publications, Tokyo, 1982).
32. Ito, E. & Takahashi, E. *J. geophys. Res.* **94,** 10637–10646 (1989).
33. Ito, E., Akaogi, M., Topor L. & Navrotsky, A. *Science* **249,** 1275–1278 (1990).
34. Masters, G., Jordan, T. H., Silver, P. G. & Gilbert, F. *Nature* **298,** 609–613 (1982).
35. Woodhouse, J. H. & Dziewonski, A. M. *J. geophys. Res.* **89,** 5953–5986 (1984).
36. Tanimoto, T. *Geophys. J. Int.* **100,** 327–336 (1990).
37. Masters, G. & Bolton, H. *Eos* **72,** 316 (1991).
38. Ekström, G., Dziewonski, A. M. & Ibañez, J. *Eos* **71,** 1462 (1990).
39. Zhou, H., Anderson, D. L. & Clayton, R. W. *J. geophys. Res.* **95,** 6799–6827 (1990).
40. Schwartz, S. Y., Lay, T. & Grand, S. P. *Geophys. Res. Lett.* **18,** 1265–1268 (1991).
41. Schwartz, S. Y., Lay, T. & Beck, S. L. *J. geophys. Res.* **96,** 14445–14460 (1991).
42. Gaherty, J. B., Lay, T. & Vidale, J. E. *J. geophys. Res.* **96,** 16349–16367 (1991).
43. Silver, P. & Chan, W. *J. geophys. Res.* **91,** 13787–13802 (1986).
44. Beck, S. L. & Lay, T. *Geophys. Res. Lett.* **13,** 1007–1010 (1986).
45. Lay, T. & Young, C. J. *Geophys. Res. Lett.* **16,** 605–608 (1989).
46. Giardini, D. & Woodhouse, J. H. *Nature* **307,** 505–509 (1984).
47. Giardini, D. & Woodhouse, J. H. *Nature* **319,** 551–555 (1986).
48. Hamburger, M. W. & Isacks, B. L. *J. geophys. Res.* **92,** 13841–13854 (1987).
49. Fitch, T. J. *Phys. Earth planet. Inter.* **26,** 156–166 (1975).
50. Frohlich, C. & Barazangi, M. *Phys. Earth planet. Inter.* **21,** 1–14 (1980).
51. Zhou, H. *Phys. Earth planet. Inter.* **61,** 199–229 (1990).
52. Sondergeld, C. H., Isacks, B. L., Barazangi, M. & Billington, S. *Bull. seismol. Soc. Am.* **67,** 537–541 (1977).
53. Bock, G. *Phys. Earth planet. Inter.* **25,** 360–371 (1981).
54. Hager, B. H. & Raefsky, A. *Eos* **62,** 1074 (1981).
55. Ringwood, A. E. & Irifune, T. *Nature* **331,** 131–136 (1988).
56. Stacey, F. D. *Physics of the Earth* (Wiley, New York, 1977).

ACKNOWLEDGEMENTS. We thank S. King, J. Phipps Morgan and R. Woodward for advice. This research was supported in part by the NSF.

Nature of biological electron transfer

Christopher C. Moser, Jonathan M. Keske, Kurt Warncke, Ramy S. Farid & P. Leslie Dutton*

The Johnson Research Foundation, Department of Biochemistry and Biophysics, University of Pennsylvania, Philadelphia, Pennsylvania 19104, USA

Powerful first-order analysis of intraprotein electron transfer is developed from electron-transfer measurements both in biological and in chemical systems. A variation of 20 Å in the distance between donors and acceptors in protein changes the electron-transfer rate by 10^{12}-fold. Protein presents a uniform electronic barrier to electron tunnelling and a uniform nuclear characteristic frequency, properties similar to an organic glass. Selection of distance, free energy and reorganization energy are sufficient to define rate and directional specificity of biological electron transfer, meeting physiological requirements in diverse systems.

In 1960 Chance and Nishimura discovered that electron transfer between a cytochrome *c* and a light-activated bacteriochlorophyll in the bacterium *Chromatium vinosum* occurred even at 80 K (ref. 1). Later DeVault and Chance[2] reported that the millisecond electron transfer was temperature-independent from 120 K to 4 K and deduced that the reaction proceeded through a quantum mechanical tunnelling mechanism, perhaps taking place over a distance as large as 30 Å. They suggested that such long-range electron transfer may be common and essential to the biological redox energetics of chloroplasts and mitochondria. This work coincided with Mitchell's development of the chemiosmotic hypothesis which proposed that the key electron-transfer steps of respiration and photosynthesis were directed across the 35 Å span of the membrane dielectric[3]. The past 25 years have seen these advances gain support and general acceptance, yet descriptions of factors that govern long-range electron transfer vital to the bioenergetic machinery have remained unclarified. The analysis we present here provides guidelines basic to the understanding of the design and engineering of respiratory and photosynthetic electron-transfer chains and other redox enzymes.

The traditional transition-state description of the rates of chemical reactions involves motion along a potential energy surface in which the reactant atoms gain energy from thermal collisions, surmount an activation energy barrier to achieve a transition state and spontaneously decay into the product. In contrast to these essentially adiabatic reactions, where formation of the transition state leads almost inevitably to the product, the probability of long-distance electron transfer between distant, weakly coupled donors and acceptors from such a transition point is small. Instead, a simple, non-adiabatic description given by Fermi's golden rule is more appropriate (equations and parameters are described in Box 1 and ref. 4). The rule states that the electron-transfer rate is proportional to the square of the (weak) coupling of the reactant and product electronic states, V_R^2, which in turn is proportional to the overlap of the donor and acceptor electronic wavefunctions across the space separating electron donor and acceptor molecules. In the simplest view, the overlap falls off exponentially with edge-to-edge distance (R), modified by a coefficient (β) which describes the contribution made by the intervening medium in propagating the wavefunction.

The nuclear positions of reacting molecules and their environment, so critical to transition state theory, have a central role in the second term of the golden rule. Calculation of this term, described as the density of states by Fermi, is problematic but can be considerably simplified by assuming the nuclei of the donor, acceptor and immediate environment act effectively as harmonic oscillators. In this case, a Franck–Condon-weighted density of states reflecting the overlap of reactant and product

* To whom correspondence should be addressed.